BMB
Reports

BMB Rep. 2016; 49(12): 681-686
www.bmbreports.org

Crystallographic snapshots of active site metal shift in *E. coli* fructose 1,6-bisphosphate aldolase

Huyen-Thi Tran[1,2,#], Seon-Hwa Lee[3,#], Thien-Hoang Ho[1], Seung-Hye Hong[3], Kim-Hung Huynh[1], Yeh-Jin Ahn[4], Deok-Kun Oh[3,] & Lin-Woo Kang[1,*]*

[1]Department of Biological Sciences, Konkuk University, Seoul 05029, Korea, [2]Department of Biotechnology and Food Technology, Industrial University of Ho Chi Minh City, 12 Nguyen Van Bao Street, Ward 4, Go Vap District, Ho Chi Minh City, Vietnam, [3]Department of Bioscience and Biotechnology, Konkuk University, Seoul 05029, Korea, [4]Department of Life Science, Sangmyung University, Seoul 03016, Korea

Fructose 1,6-bisphosphate aldolase (FBA) is important for both glycolysis and gluconeogenesis in life. Class II (zinc dependent) FBA is an attractive target for the development of antibiotics against protozoa, bacteria, and fungi, and is also widely used to produce various high-value stereoisomers in the chemical and pharmaceutical industry. In this study, the crystal structures of class II *Escherichia coli* FBA (*Ec*FBA) were determined from four different crystals, with resolutions between 1.8 Å and 2.0 Å. Native *Ec*FBA structures showed two separate sites of Zn1 (interior position) and Zn2 (active site surface position) for Zn^{2+} ion. Citrate and TRIS bound *Ec*FBA structures showed Zn^{2+} position exclusively at Zn2. Crystallographic snapshots of *Ec*FBA structures with and without ligand binding proposed the rationale of metal shift at the active site, which might be a hidden mechanism to keep the trace metal cofactor Zn^{2+} within *Ec*FBA without losing it. [BMB Reports 2016; 49(12): 681-686]

INTRODUCTION

Fructose 1,6-bisphosphate aldolase (FBA; E.C. 4.1.2.13) catalyzes the second reversible step of the glycolytic pathway, which is the hydrolysis of the open-chain form of fructose 1,6-bisphosphate (FBP) to glyceraldehyde 3-phosphate (G3P) and dihydroxyacetone phosphate (DHAP). There are two known families of FBA - class I and class II. Although both classes adopt similar α/β folds, they have different catalytic components at the active site. Class I FBAs use a Schiff-base (imine, containing carbon-nitrogen double bond) linkage between the active site Lys residue and the substrate C(2) carbonyl group (1). Class II FBAs use inorganic cofactor of zinc ion at the active site to bind and catalyze substrates; the divalent zinc ion coordinates both C(2) carbonyl and C(3) hydroxyl oxygen atoms of substrate (2) (Fig. 1A).

The class I FBAs are mostly distributed in mammals, whereas class II FBAs are only found in protozoa, bacteria, fungi, and blue-green algae. The necessity of class II FBAs in *Mycobacterium tuberculosis*, *Escherichia coli* (*E. coli*), and *Streptomyces galbus* (3-6) makes this class an attractive target for the development of antibiotics. In addition to the essential roles of FBAs in diverse catabolic and anabolic processes within cells, they have also been widely used in the chemical and pharmaceutical industry to produce various high value stereoisomers of carbohydrates, amino acids, and hydroxylated molecules (7-9).

Previously determined crystal structures of *Ec*FBA alone, and in complex with transition-state analog (phosphoglycolohydroxamate, PGH), showed two mutually exclusive metal binding sites at the active site (2, 10). In *Giardia lamblia*, the substrate fructose 1,6-bisphosphate (FBP)-bound FBA structure was determined, and a substrate-binding induced metal shift was proposed (11). Studies of developing specific inhibitors against FBAs have been carried out (12, 13). In both mechanistic studies and inhibitor development for new antibiotics, the position and coordination of the catalytic metal ion is essential.

In this study, we determined four different crystal structures (1.8 Å to 2.0 Å) of class II *Ec*FBA. The crystallographic snapshots of *Ec*FBA structures show three different metal-binding states at two sites, having different metal-coordinating environments, which provide the detail mechanism of active site metal shift.

*Corresponding authors. Lin-Woo Kang, Tel: +82-2-450-4090; Fax: +82-2-444-6707; E-mail: lkang@konkuk.ac.kr, Deok-Kun Oh, Tel: +82-2-450-4118; Fax: +82-3437-6106; E-mail: deokkun@konkuk.ac.kr
#These authors contributed equally to this work.

https://doi.org/10.5483/BMBRep.2016.49.12.132

Received 4 August 2016, Revised 30 August 2016, Accepted 10 October 2016

Keywords: Class II fructose 1,6-bisphosphate aldolase, Inorganic cofactor, Metal ion, X-ray crystallography

ISSN: 1976-670X (electronic edition)

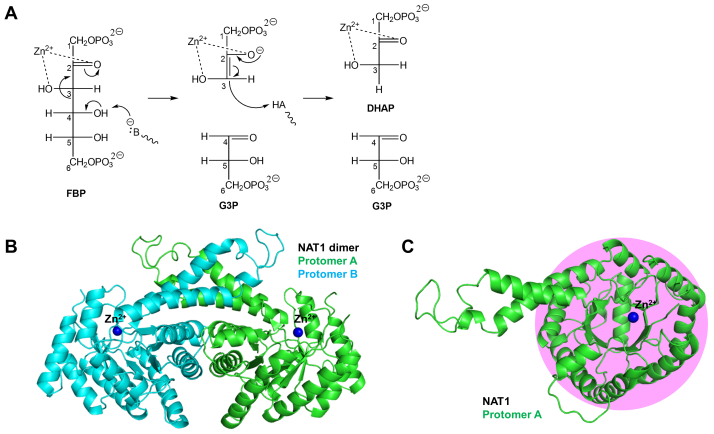

Fig. 1. Mechanism and structure of *Ec*FBA. (A) Catalytic mechanism of *Ec*FBA. (B) Overall native structure of *Ec*FBA dimer (NAT1). (C) Protomer *Ec*FBA structure showing the TIM barrel fold (pink shade) viewed from the top.

RESULTS

Overall structure of *Ec*FBA

*Apo-Ec*FBA is present as a dimer in the asymmetric unit; its structure is well conserved, when compared to the previously published structure (10). Each protomer has the conserved $(\alpha/\beta)_8$ barrel fold of other class II FBAs (Fig. 1B and 1C). Dimerization takes place on the surface of outer helices (α2 and α4) of the TIM barrel fold with the additional help of two protruded long helices (α10 and α11) (Fig. S1). Most of the 359 amino acids in *Ec*FBA show good electron density, except for residues 178-195 and 224-235 (Table S1).

As expected, the active site of *Ec*FBA was located at the C-terminal end of the TIM barrel. Till date, no substrate or product bound *Ec*FBA structures are available, and only the reaction intermediate analog phosphoglycolohydroxamate (PGH)-bound *Ec*FBA structure has been determined (2). Since past few years, our group has been studying to determine the substrate, product, or reaction intermediate-bound *Ec*FBA structures. From the trials, we collected several tens of X-ray diffraction datasets from *Ec*FBA crystals soaked with substrate or ligands such as fructose 1,6-bisphosphate, tagatose 1,6-phosphate, and dihydroxyacetone. However, most turned out to be just native *Ec*FBA structures without ligand binding, and we were unable to obtain the reaction related ligand bound *Ec*FBA structure. Nonetheless, *Ec*FBA structures in complex with either citrate or TRIS were unexpectedly determined.

The FBA (*Gl*FBA) structures of native, FBP-bound, and tagatose 1,6-bisphosphate-bound were determined in *Giardia lamblia* (11), and the citrate-bound FBA (*Sa*FBA) structure was determined in *Staphylococcus aureus* (14); the *Gl*FBA and *Sa*FBA have sequence identities of 24.3% and 27.5%, respectively, with *Ec*FBA (Fig. S1). When we superimposed *Ec*FBA structure onto *Gl*FBA (PDB ID: 3GB6) and *Sa*FBA (PDB ID: 4TO8) structures, the overall fold and TIM barrel structure was well conserved, but the loop regions showed differences (Fig. S2). The RMSD value of the overall protomer structure between *Ec*FBA and *Gl*FBA, and between *Ec*FBA and *Sa*FBA, are 1.67 Å in 238 residues and 1.60 Å in 250 residues, respectively. The RMSD value of core TIM barrel structure between *Ec*FBA and *Gl*FBA, and *Ec*FBA and *Sa*FBA, are 1.76 Å in 139 residues and 1.50 Å in 139 residues, respectively.

In *Ec*FBA, two metal sites were located at the C-terminal side of the β-barrel structure of each protomer, separated by a distance of 3.7 Å. One site (termed 'Zn1') was at the interior of protein and the other site (termed 'Zn2') existed on the active site surface.

Metal binding and coordination in FBA structures

Previously, Blom *et al*. reported an *Ec*FBA structure (PDB ID: 1DOS), which had two mutually exclusive Zn^{2+} binding sites (10). In this study, we determined almost the same two metal-binding sites in *Ec*FBA structures from four different datasets. The crystallographic snapshots of *Ec*FBA structures show the clear tendency that the metal site having more coordinations has the stronger electron density of metal. We classified the datasets into three different metal-binding states: 1) Zn^{2+} ion exclusively bound at the interior (Zn1) of *Ec*FBA, 2) Zn^{2+} ion partially bound at both the interior (Zn1) and the active site surface (Zn2) of *Ec*FBA, and 3) Zn^{2+} ion exclusively bound at the active site surface (Zn2) of *Ec*FBA (Fig. 2).

Native *Ec*FBA structures

Both metal-binding sites were observed in two native *Ec*FBA structures (NAT1 and NAT2). In NAT1, Zn1 consisted of three His residues (His110, His226, and His264) and Glu174 (Fig. 2A). In NAT2, Zn2 consisted of two His residues (His110 and His264) (Fig. 2B). The three His and one Glu residues are strictly conserved in class II FBAs (Fig. S1). The imidazole rings of His110 and His264 could form a H-bond with Zn^{2+} ion at both sites. The electron density of the metal ion was stronger than that expected for sodium ion, and weaker than that for zinc ion at full occupancy. We calculated the occupancy of zinc ion at both sites, and placed zinc ions with partial

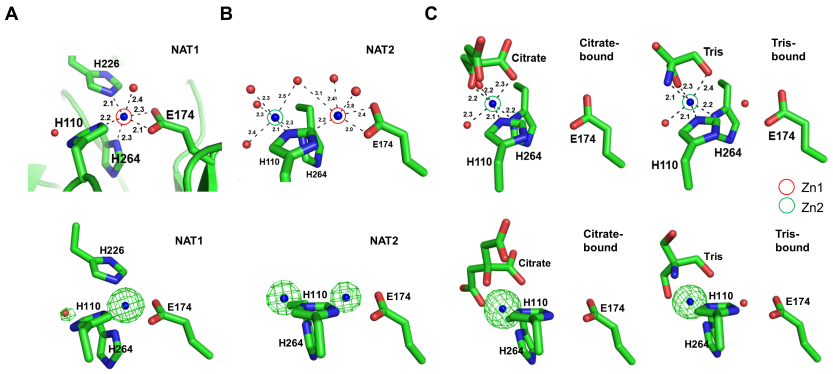

Fig. 2. Crystallographic snapshots of three different metal-binding states of *Ec*FBA. (A) Only Zn1 was occupied in NAT1 structure. (B) Both Zn1 and Zn2 were partially occupied in NAT2 structure. (C) Only Zn2 was occupied in citrate (left) or TRIS-bound (right) structures. Upper figures show stick representations of Zn1 and Zn2 in active site, and lower figures show omit maps (contoured at 10.0 σ; green) of Zn^{2+} in Zn1 and Zn2.

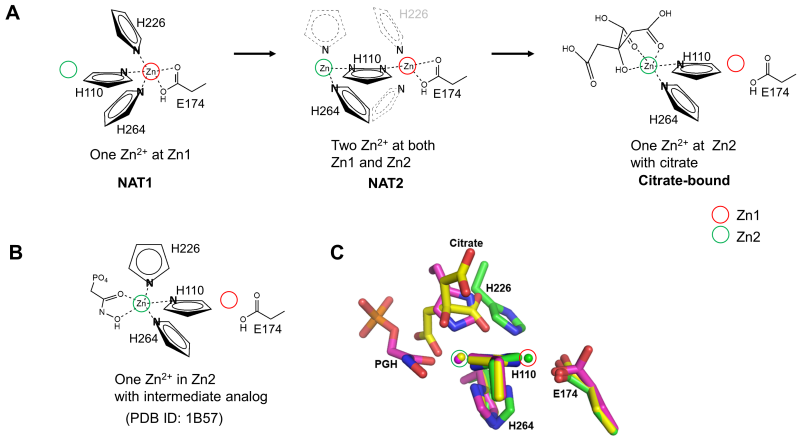

Fig. 3. Metal-binding site structures of *Ec*FBA. (A) Schematic drawing of metal shift in the *Ec*FBA active site with corresponding conformational changes of coordinating residues. Only coordinating nitrogen atom in histidine residues is shown. In NAT2 structure, flip-flop dual conformations of His110 are shown as two nitrogen atoms in a single imidazole ring. His226 residue is not shown due to disordered conformations, and the proposed positions are represented with grey dashed lines. His264 residue is shown as dual conformations to coordinate Zn^{2+} at Zn1 or Zn2. (B) Schematic drawing of phosphoglycolohydroxamate (PGH)-bound *Ec*FBA structure (2). (C) Comparison between native and ligand-bound *Ec*FBA structures. Superimposed active site structures between NAT1 (green), citrate-bound (yellow), and phosphoglycolohydroxamate (PGH)-bound (purple) *Ec*FBA structures.

occupancy at both sites (Table S2).

In the NAT1 structure, zinc ion was hexacoordinated; His110, His226, and Glu174 (bifurcated hydrogen bonds) coordinated the zinc ion in-plane, while a water molecule and His264 coordinated above and below (Fig. 2A). In the NAT2 structure, two zinc ions were positioned at Zn1 and Zn2, with only two coordinating His residues; the His226 was missing from disordered structure (Fig. 2B). The coordination at Zn2 involved His110 and a 'rotated conformation' of His264, together with four water molecules. In order to coordinate both Zn1 and Zn2, His110 sidechain could adopt a mixed 'flip-flop' state and His264 showed dual rotated conformations. Both of His110 and His264 residues were positioned as dual conformations with partial occupancy.

Citrate-bound and TRIS-bound *Ec*FBA structures

Citrate was present at a high concentration of 0.1 M in the crystallization condition of citrate-bound *Ec*FBA structure. Changing the buffer to TRIS also led to the TRIS bound structure. In the citrate-bound structure, zinc ion was bound at Zn2, where it was hexacoordinated with two His residues (His110 and His264), three oxygen atoms from the citrate molecule, and a water molecule (Fig. 2C). One conformation of His264 existed that faced the Zn2. His226 was not visible in the electron density maps. In the TRIS-bound structure, zinc ion at Zn2 was bound in a similar way as that in the citrate-bound structure, except that the two oxygen atoms and one nitrogen atom of TRIS replaced the three oxygen atoms of citrate (Fig. 2C).

Comparison of *Ec*FBA structures

We superimposed the determined *Ec*FBA structures to identify any conformational changes (Table S3). We observed that the overall structures and positions of both Zn^{2+} binding sites were well conserved in all structures. The imidazole ring plane of His110 was parallel to the two metal sites. Two other coordinating His residues of His264 (below the metal ion) and His226 (above the metal ion) changed their conformation depending on the corresponding coordinating metal ion; His264 changed the conformation towards the coordinating Zn^{2+} ion, and His226 was visible only when coordinating Zn1. The citrate or TRIS-binding site partially overlapped with His226 coordinating Zn2 (Fig. 3C). When we superimposed the PGH-bound *Ec*FBA structure [PDB ID: 1B57 (2)], His226 coordinated Zn2 at the same position occupied by either citrate or TRIS. In the PGH-bound structure, Zn2 was penta-coordinated by three His residues (His110, His226, and His264) and two oxygen atoms from PGH (Fig. 3B).

DISCUSSION

A divalent metal ion plays an essential role in the catalysis of class II FBAs. In this study, three different states of metal binding and coordination were observed in the *Ec*FBA structures, accompanied by conformational changes in the corresponding coordinating residues (Fig. 2 and 3A). The crystallographic snapshots of *Ec*FBA structures suggest the detail mechanism of metal shift between two sites.

Zn1 and Zn2 intrinsically have five and three coordinating electron donors, respectively. Three coordinators were the same His residues shared at both Zn1 and Zn2, showing conformational changes. The additional two coordinators at Zn1 were the bifurcated side chain of Glu174 residue. Therefore, the preferential coordination of the three His residues at one site will diminish the coordination at the other site. When we compared NAT1 structure with NAT2 structure, one coordinating residue (His226) in Zn1 was lost in the NAT2 structure, thus decreasing the metal-binding affinity at Zn1, and making it easier for Zn^{2+} from Zn1 to move to Zn2 with the rotation of His264 to Zn2. We determined two ligand (citrate or TRIS)-bound *Ec*FBA structures, and both substrate-mimicking ligands coordinated Zn2. Zn2 existed on the active site surface of the protein and had only two possible coordinating His residues of His110 and His264 in *apo-Ec*FBA, considering flexible His226. In the Zn2 of *apo-Ec*FBA, additional metal coordinating positions should be left unoccupied for substrate binding. Binding of substrate at the active site provides two additional metal coordinating electron donors at Zn2. When Zn^{2+} moves from Zn1 to Zn2 with conformational changes of His110 and His264, the metal coordination at Zn2 gets stronger; at the same time, that of Zn1 gets weaker (Fig. 4). The enhanced Zn^{2+} binding at Zn2 diminishes the metal-binding affinity of Zn1. In the ligand-bound *Ec*FBA structures, no Zn^{2+} was bound at Zn1. In both *Gl*FBA and *Sa*FBA structures, Zn1 and Zn2 were conserved; the zinc ion binds at Zn1 without ligand and at Zn2 with ligand (Fig. S3), which corresponds with the *Ec*FBA structures in this study.

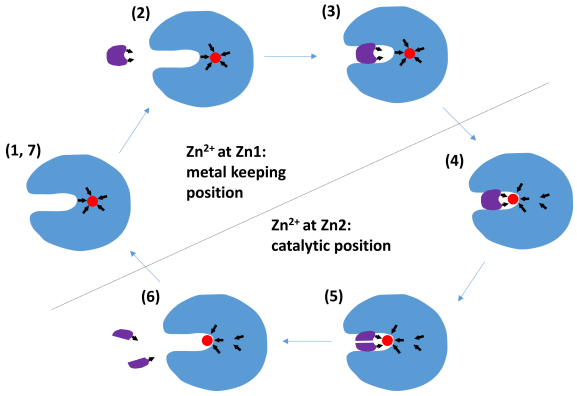

Fig. 4. Proposed mechanism of active site Zn^{2+} movement in *Ec*FBA. (1) Native *Ec*FBA structure with a metal ion at the interior protein (Zn1). (2) The substrate contains a metal-coordinating motif. The active site surface also contains a metal-binding site (Zn2). (3) When substrate binds at active site, Zn2 is formed with more electronegative coordinators. (4) The completely formed Zn2 recruits a metal ion from Zn1 to Zn2. (5) The active form of *Ec*FBA performs catalytic reaction. (6) Products are released from the active site and metal ion at Zn2 loses parts of coordination that had been provided by the substrate. (7) Metal ion at Zn2 returns to Zn1, which has more complete coordination at the interior of the protein. The arrows show the direction of coordination by His and Glu residues and substrate.

We speculate that Zn1 might be a reservoir for trace metal Zn^{2+}. Zn2 is exposed to solution because Zn^{2+} should directly interact with substrate and perform catalysis, of which the minimal coordination geometry without substrate-binding could risk the loss of the valuable trace metal Zn^{2+} from *Ec*FBA. The conditional shift of the metal cofactor to the inner position with more secure coordination of *Ec*FBA, could be helpful to keep the essential metal cofactor within the enzyme. The detail metal shift mechanism will be useful for better understanding the catalytic mechanism of *Ec*FBA, and possibly of general FBAs.

MATERIALS AND METHODS

Gene cloning

The D-fructose-1,6-bisphosphate aldolase (*fbaA*, GI: 16130826) gene encodes 359 amino acid residues. The cloning of *fbaA* gene was carried out with the normally used method (15). *fbaA* was amplified by PCR using genomic DNA isolated from *E. coli* K-12, using a genomic DNA extraction kit (GeneAll, Seoul, Korea). The forward and reverse primers for *fbaA* contained SalI and NotI restriction sites (underlined): 5'-GTCGACATGTCTAAGATTTT TGATTTCGTAAAACC-3' and

5'-ATAATGCGGCCGCTTACAGAACGTCGATCGCGTT-3'. DNA fragments obtained by PCR amplification with *Taq* polymerase (Bioneer, Alameda, CA, USA) were purified using a PCR purification kit (Qiagen, Valencia, CA, USA) and ligated into the pRSF-duet-1 vector (Novagen, Madison, WI, USA), which was then transformed into *E. coli* ER2566 cells and plated on Luria-Bertani (LB) agar containing 0.1 mM kanamycin. A kanamycin-resistant colony was selected, and its plasmid was sequenced using a DNA analyzer (ABI Prism 3730xl; Perkin-Elmer, Waltham, MA, USA).

Overexpression and purification

The *Ec*FBA was expressed and purified with the normally used recombinant protein expression and purification method (16). The recombinant *E. coli* cells were cultured at 37°C in a 2 L-flask containing 500 ml of LB medium and 0.1 mM kanamycin, while being shaken at 200 rpm. When the optical density of the bacterial culture reached 0.6 at 600 nm, isopropyl-β-D thiogalactopyranoside (IPTG) was added to a final concentration of 0.1 mM, inducing *Ec*FBA expression. Following this, the culture was incubated on a shaker for a further 16 h at 16°C, at 150 rpm. Cells were harvested from the culture broth by centrifugation at 6,000×*g* for 30 min (4°C) and re-suspended in 50 mM phosphate buffer (pH 8.0) containing 300 mM NaCl, 10 mM imidazole, and a protease inhibitor (0.1 mM phenylmethylsulfonyl fluoride). The re-suspended cells were disrupted by sonication, on an ice bath. The cell debris was removed by centrifugation at 1,3000×*g* for 20 min (4°C), and the supernatant was filtered through a 0.45-μm filter. The filtrate was applied to an immobilized metal ion affinity chromatography (IMAC) cartridge (Bio-Rad) equilibrated with 50 mM phosphate buffer (pH 8) containing 300 mM KCl. The column was washed extensively with 50 mM phosphate buffer (pH 8) containing 300 mM KCl and 30 mM imidazole, and the bound protein was eluted with 50 mM phosphate buffer (pH 8) containing 300 mM KCl and 300 mM imidazole, at a flow rate of 1 ml/min. The active fractions were collected and dialyzed in 50 mM Tris-HCl buffer (pH 8.5). After dialysis, the resulting solution contained the purified enzyme that was used for crystallization trials. The affinity purification tag from the expression vector was not cleaved off, and was retained in the purified enzyme. A standard Bradford assay was used to determine protein concentration. Protein expression was evaluated by SDS-PAGE.

Crystallization and X-ray data collection

Initial crystallization was carried out at 287 K in 96-well plates (Intelli-Plates, Art Robbins, USA), using the sitting-drop vapor diffusion method. An automated pipetting system (Hydra II E-drop, Matrix) was used with screening kits from Hampton Research and Emerald Biosystems. The drops consisted of 0.5 μl protein solution (10 mg/ml in 20 mM Tris, pH 7.0) and 0.5 μl reservoir solution; these were then equilibrated against 70 μl reservoir solution at 14°C. After 3 days, nascent thin planar *Ec*FBA crystals were observed in 'Hampton Crystal Screen Lite condition No. 09' (15% PEG 4000, 0.2 M ammonium acetate, and 0.1 M sodium citrate tribasic dihydrate, pH 5.6). These crystals were reproduced using hanging drops consisting of 0.9 μl of protein solution mixed with 0.9 μl of reservoir solution. Each hanging drop was positioned over 1 ml of the reservoir solution. Crystals were optimized by varying the PEG concentration and by assessing four buffers (sodium citrate, HEPES, TRIS, Bis-TRIS, and MES). Thick planar *Ec*FBA crystals were obtained in reservoir solutions consisting of 0.2 M ammonium acetate, 15% PEG 4000 and 0.1 M of any the four buffers listed (above), covering a range of pH values from 5.5 to 7.0. However, most fully grown crystals were seen at pH 7.0. Potassium chloride (10 mM) was added to the reservoir solutions for soaking ligands of substrate fructose 1,6-bisphosphate or inhibitor tagatose 1,6-bisphosphate into *apo-Ec*FBA crystals. All crystals were cryoprotected with 20% (v/v) glycerol, and then flash-cooled at 100 K in liquid nitrogen. X ray diffraction data were collected from the crystals on beamline 5C, Pohang Accelerator Laboratory (PAL, Republic of Korea), using an ADSC Q315r CCD detector. The data were integrated and scaled using *DENZO* and *SCALEPACK*, respectively.

Structure determination and refinement

The *apo* structure of *Ec*FBA was determined by molecular replacement using *Phaser*-MR from the CCP4 software package (17), using the 1.6 Å structure of *Ec*FBA (PDB: 1DOS) having a 99.7% sequence identity, as a template model. Construction of both the model and electron density was performed in *COOT* (18). The resulting model was refined using *Refmac5* in the CCP4 package (19). The *apo-Ec*FBA structure was employed as a template for determining the other *Ec*FBA structures by molecular replacement. The occupancy of metal ion was calculated in *PHENIX* (20). The resulting structures were validated in *PROCHECK* (21). The statistics of structure refinement are summarized in Table S1. Root-mean-square deviation values for the superimposed structures were calculated using the *GESAMT* tool (22) in 'Superpose Molecules' in the CCP4 software suite. Structures were displayed using *PyMOL* (23). Structure-based multiple sequence alignment was performed in *T-Coffee* (24), and then presented using the *ESPript* server (25). The determined *Ec*FBA structures were deposited in the Protein Data Bank (PDB): NAT1 structure (crystal I) was deposited as 5GK3, NAT2 structure (crystal II) as 5GK4, Citrate-bound structure as 5GK6, and Tris-bound structure as 5GK7.

ACKNOWLEDGEMENTS

We are grateful to the staff members of Beamline 5C at the Pohang Accelerator Laboratory (PAL), Republic of Korea. This paper was supported by Konkuk University in 2014.

REFERENCES

1. Lorentzen E, Siebers B, Hensel R and Pohl E (2005) Crystal structure of an archaeal class I aldolase and the evolution of (betaalpha)8 barrel proteins. Biochemistry 44, 4222-4229
2. Hall DR, Leonard GA, Reed CD, Watt CI, Berry A and Hunter WN (1999) The crystal structure of Escherichia coli class II fructose-1, 6-bisphosphate aldolase in complex with phosphoglycolohydroxamate reveals details of mechanism and specificity. J Mol Biol 287, 383-394
3. Marsh JJ and Lebherz HG (1992) Fructose-bisphosphate aldolases: an evolutionary history. Trends Biochem Sci 17, 110-113
4. Pegan SD, Rukseree K, Franzblau SG and Mesecar AD (2009) Structural basis for catalysis of a tetrameric class IIa fructose 1,6-bisphosphate aldolase from Mycobacterium tuberculosis. J Mol Biol 386, 1038-1053
5. Gerdes SY, Scholle MD, Campbell JW et al (2003) Experimental determination and system level analysis of essential genes in Escherichia coli MG1655. J Bacteriol 185, 5673-5684
6. Wehmeier UF (2001) Molecular cloning, nucleotide sequence and structural analysis of the Streptomyces galbus DSM40480 fda gene: the S. galbus fructose-1,6-bisphosphate aldolase is a member of the class II aldolases. FEMS Microbiol Lett 197, 53-58
7. Wagner J, Lerner RA and Barbas CF (1995) Efficient aldolase catalytic antibodies that use the enamine mechanism of natural enzymes. Science 270, 1797-1800
8. Von der Osten CH, Sinskey AJ, Barbas CF, Pederson RL, Wang YF and Wong CH (1989) Use of a recombinant bacterial fructose-1, 6-diphosphate aldolase in aldol reactions: preparative syntheses of 1-deoxynojirimycin, 1-deoxymannojirimycin, 1, 4-dideoxy-1, 4-imino-D-arabinitol, and fagomine. J Am Chem Soc 111, 3924-3927
9. Liu J, Hsu C-C and Wong C-H (2004) Sequential aldol condensation catalyzed by DERA mutant Ser238Asp and a formal total synthesis of atorvastatin. Tetrahedron Lett 45, 2439-2441
10. Blom NS, Tetreault S, Coulombe R and Sygusch J (1996) Novel active site in Escherichia coli fructose 1,6-bisphosphate aldolase. Nat Struct Biol 3, 856-862
11. Galkin A, Li Z, Li L et al (2009) Structural insights into the substrate binding and stereoselectivity of giardia fructose-1,6-bisphosphate aldolase Biochemistry 48, 3186-3196
12. Daher R, Coincon M, Fonvielle M et al (2010) Rational design, synthesis, and evaluation of new selective inhibitors of microbial class II (zinc dependent) fructose bis-phosphate aldolases. J Med Chem 53, 7836-7842
13. Capodagli GC, Sedhom WG, Jackson M, Ahrendt KA and Pegan SD (2014) A noncompetitive inhibitor for Mycobacterium tuberculosis's class IIa fructose 1,6-bisphosphate aldolase. Biochemistry 53, 202-213
14. Capodagli GC, Lee SA, Boehm KJ, Brady KM and Pegan SD (2014) Structural and functional characterization of methicillin-resistant Staphylococcus aureus's class IIb fructose 1,6-bisphosphate aldolase. Biochemistry 53, 7604-7614
15. Lee SJ, Jang JH, Yoon GY et al (2016) Mycobacterium abscessus D-alanyl-D-alanine dipeptidase induces the maturation of dendritic cells and promotes Th1-biased immunity. BMB Rep 49, 554-559
16. Kim JH, Choi JS, Kim S et al (2015) Synergistic effect of two E2 ubiquitin conjugating enzymes in SCF(hFBH1) catalyzed polyubiquitination. BMB Rep 48, 25-29
17. Winn MD, Ballard CC, Cowtan KD et al (2011) Overview of the CCP4 suite and current developments. Acta Crystallogr D Biol Crystallogr 67, 235-242
18. Emsley P, Lohkamp B, Scott WG and Cowtan K (2010) Features and development of Coot. Acta Crystallogr D Biol Crystallogr 66, 486-501
19. Murshudov GN, Skubak P, Lebedev AA et al (2011) REFMAC5 for the refinement of macromolecular crystal structures Acta Crystallogr D Biol Crystallogr 67, 355-367
20. Afonine PV, Grosse-Kunstleve RW, Echols N et al (2012) Towards automated crystallographic structure refinement with phenix.refine. Acta Crystallogr D Biol Crystallogr 68, 352-367
21. Laskowski R, MacArthur M, Moss D and Thornton J (1993) PROCHECK: A program to check the stereochemical quality of protein structures. J Appl Cryst 26, 283-291
22. Krissinel E (2012) Enhanced fold recognition using efficient short fragment clustering. J Mol Biochem 1, 76-85
23. Schrodinger L (2010) The PyMOL Molecular Graphics System, Version 1.3r1.
24. Notredame C, Higgins DG and Heringa J (2000) T-Coffee: A novel method for fast and accurate multiple sequence alignment. J Mol Biol 302, 205-217
25. Gouet P CESD and Metoz F (1999) ESPript: multiple sequence alignments in PostScript. Bioinformatic 15, 305-308